Smoke Dispersion from Multiple Fire Plumes

J. Trelles, K. B. McGrattan, H. R. Baum

Smoke Dispersion from Multiple Fire Plumes

Javier Trelles,* Kevin B. McGrattan,[†] and Howard R. Baum[‡]

National Institute of Standards and Technology, Gaithersburg, Maryland 20899

The effects of multiple fire plumes in a stably stratified atmosphere with a uniform wind are investigated. A parabolized approximation of the steady-state Navier–Stokes equations obtained by replacing the windward velocity component with the ambient wind speed is the basis of the model. Lagrangian particles are used to visualize the flow, account for atmospheric fluctuations, and determine the smoke concentration field. Multiple-plume interactions can push particulate up to altitudes exceeding that of an equivalent single plume. A parametric study based on separation and heat release rates is performed for two plumes. The most dramatic increases in plume rise and spread are found for in-line plumes, parallel to the wind direction. Multiple-plume interactions can yield nonuniformities in the smoke concentration field that differ substantially from that predicted by Gaussian models.

Nomenclature

c_p = specific heat coefficient for air at constant pressure, J/(kg · K)
$\hat{e}_j$ = unit vector in the j direction
F_N = $F_N(\mu, \sigma)$ is a normally distributed random function with mean μ and standard deviation σ
f = stretching factor
g = acceleration of gravity, 9.81 m/s²
$\mathbf{g}$ = acceleration of gravity vector, $-g\hat{e}_z$, m/s²
$\mathcal{H}$ = total pressure head, Pa
h = mixing height, m
k = coefficient of eddy thermal conductivity, W/(m · K)
L = characteristic length, m
M = total particulate mass flow rate, kg/s
M_i = particulate mass flow rate for the ith fire, kg/s
N_0^2 = square of the Brunt–Väisälä frequency, $(g/\theta_0)(d\theta_0/dz) = (g/T_0)(dT_0/dz + g/c_p)$, 1/s²
n = total number of particles
n_f = number of fires
n_i = number of particles in the ith plume
Pr = turbulent Prandtl number, $\mu c_p/k$
p = pressure, Pa
Q = total heat release rate, W
Q_i = heat release rate for the ith fire, W
$\dot{q}$ = heat release rate per unit volume, W/m³
$\mathcal{R}$ = universal gas constant, J/(kg · K)
R_j = Lagrangian correlation coefficient for the j component of velocity
Re = turbulent Reynolds number, $f^2 \rho V L/\mu$
r_j = distance from the j-direction cell center, expressed as a fractions of the cell dimensions
s = distance in the horizontal plane between fires, m
T = temperature, K
$\bar{T}_{TOT}^*$ = half-plane integral of the temperature field, defined as $\iint \bar{T}^* \, dy^* \, dz^* / \iint dy^* \, dz^*$
t = time, s
U_∞ = ambient wind, m/s
u = x component of the velocity, m/s
$\mathbf{u}$ = velocity vector in the y–z plane (v, w), m/s
V = characteristic velocity of the air in the crosswind plane, m/s
v = y component of the velocity, m/s

w = z component of the velocity, m/s
x = first Cartesian coordinate, m
$\mathbf{x}$ = position vector (x, y, z), m
y = second Cartesian coordinate, m
$y_{\bar{T}*}^*$ = the y moment of the temperature field, defined as $\iint y^* \bar{T}^* \, dy^* \, dz^* / \iint dy^* \, dz^*$
z = third Cartesian coordinate, m
$z_{\bar{T}*}^*$ = the z moment of the temperature field, defined as $\iint z^* \bar{T}^* \, dy^* \, dz^* / \iint dy^* \, dz^*$
β_j = plume cross-sectional half-width in the j direction, m
Γ = lapse rate, °C/km
ε_{CFL} = user-chosen stability tolerance
θ = potential temperature, $T(p_\infty/p)^{R/c_p}$, K
μ = coefficient of eddy viscosity, kg/(m · s)
ρ = density, kg/m³
ρ_P = smoke concentration, μg/m³
σ_v, σ_w = turbulent fluctuations for the v and w velocity components, respectively, m/s
$\sigma_\theta, \sigma_\phi$ = turbulent fluctuations in the y and z directions, respectively
τ = atmospheric relaxation time, s
ω = vorticity, x component, 1/s
$\boldsymbol{\omega}$ = vorticity vector, 1/s
∇ = gradient in the y–z plane, 1/m

Subscripts

p = referring to particulate quantities
0 = quantity that only depends on z
∞ = ground level, ambient condition

Superscripts

0 = initial distribution for a computational variable
$\sim$ = perturbation quantity
$\cdot$ = quantity per unit time
$*$ = dimensionless variable
$\prime$ = turbulent fluctuation quantity

I. Introduction

LARGE-SCALE fire scenarios commonly involve multiple combustion sources interacting with a nonstationary atmosphere. Examples include the burning of oil spills on water,[1] urban mass fires,[2] and a variety of industrial accidents. The multiple plumes distribute combustion products over large areas while the plume interactions can produce strong aerodynamic forces. These interactions can have unexpected results on the containment of airborne material. The mixing promoted by the large-scale plume vortex structures can transport combustion products to areas that would not have been covered by a single plume produced by a fire

whose heat output equals the sum of the multiple fires. This paper investigates multiple fire plumes to arrive at a better understanding of these phenomena. The mathematical model used in this investigation offers increased realism over previous integral models that do not adequately describe fire-induced buoyancy forces. The model is designed to produce high-resolution simulations of the mixing in the transition region where the smoke transport goes from a fire-induced to an atmospheric turbulence dominated domain. The class of problems considered excludes fires large enough to alter the prevailing atmosphere; it allows for fires sufficiently strong to interact with each other and to have local atmospheric influence.

There have been two approaches to modeling wind-blown multiple-plume scenarios: integral methods, which reduce the problem to a set of ordinary differential equations to be solved either numerically, with an approximate expression, or with an empirical fit, and field models based on the partial differential equations of motion, requiring computational fluid dynamics (CFD) techniques for solution. Integral methods based on Gaussian profiles that evolve along curved center-line coordinates are by far the most common ways used in the past to model the problem of interest.

Multiple-plume integral models can be sorted into three categories. The first, termed a resultant plume model, substitutes a single, equivalent plume, which conserves important but not universally agreed on physical quantities such as mass flux, thermal energy flux, and mechanical energy flux for a set of plumes. References 3–6 take this approach. The second category can be described as a corrected, overlapping plume model. In this approach, plume profiles are superimposed, taking pertinent flow properties and source distributions into account without accounting for the individual plume's ability to entrain the other. References 7–11 used zone modeling to describe the different stages of multiple-plume evolution. Wood and associates[12–14] use superposition with local corrections. The KUMULUS model[15,16] employs an elaborate conglomeration methodology for plumes within a certain distance of each other and then sums over these combinations to obtain concentrations at a point. The third category, called a merging plume model, attempts smooth plume interaction until independent or fully merged plumes are attained. Wu and Koh[17] provided an example.

All of these approaches suffer from the inability to describe the plume shapes in regions where interaction is occurring. Furthermore, many integral models, such as KUMULUS,[15,16] are limited to two-dimensional calculations in a specified vertical plane that is parallel to the wind. Attempts to account for more realistic scenarios lead to greater numerical complexity and to application-specific tuning or calibration as well. Hence, their predictive power is limited.

Because attempts at greater realism lead to integral models that are only tractable numerically, the rapid improvements in computers and CFD techniques have made models based on the underlying fluid mechanical equations the preferred approach. Although it seems within the capabilities of published field models to address the multiple-plume problem, this emphasis appears not to have been pursued to date. The analysis presented here is based on extensions of the numerical work in Refs. 18 and 19 for single plumes such as that shown in Fig. 1. The same governing equations were solved using a different numerical approach by Ghoniem et al.[20] and Zhang and Ghoniem,[21–23] who strongly emphasized vortex dynamics studies but have not extended their approach to multiple plumes. This paper focuses on particulate dynamics in a multiple-plume environment.

The goals of the present effort are to introduce the numerical model and to use it to study the effects of multiple-fire-plume interactions. In Sec. II, the assumptions behind this model are stated. The resulting governing equations are presented. Scaling appropriate for multiple-plume scenarios is introduced. These derived characteristic quantities are used to nondimensionalize the governing equations, preparing the mathematical model for numerical integration. In Sec. III, the techniques used to solve the equations are discussed along with the associated error estimates. The CPU times for different resolution runs is presented. The physics of the single plume used for the benchmarking studies is also described. In Sec. IV, two-plume interactions are considered in detail. The angle and the nondimensional separation distance between introduction points suffice to characterize the interaction of two plumes of equal fire strength. Criteria for independent plumes are established.

Comparisons with an equivalent single plume are made. In Sec. V, three-plume and eight-plume examples are presented to illustrate the rich and unusual dynamics available from multiple-plume scenarios. Implications from these examples to actual applications are discussed.

II. Mathematical Model

The steady-state equations that describe the plume dynamics are based on the Boussinesq form of the Navier–Stokes equations. The prevailing windward component of the velocity is replaced by a constant ambient wind. The crosswind components are subject to slight variations characteristic of atmospheric turbulence. This approximation is widely used in the study of aircraft wake dynamics that have many features analogous to those described here. After these simplifications, described in more detail next, the three-dimensional, steady-state system of equations becomes equivalent to a two-dimensional, time-dependent system. It can now be characterized as an initial value problem in which the initial solution is prescribed in a plane perpendicular to the direction of the prevailing wind. This initial plane is taken to be a few fire diameters downwind of the fire. The simplified equations resulting from these assumptions can be solved in sufficient detail to resolve the plume rise down to a length scale in the range of 10 m within a domain several kilometers on a side. This is sufficient to capture the entrainment of air into the smoke plume and to describe the plume rise over flat terrain, as is shown in Fig. 1.

The Boussinesq approximation assumes that, several diameters downstream of the fire, the induced temperature and density differences are a small fraction of their ambient ground-level values.[24] The pressure is divided into a hydrostatic term p_0 and a fire-induced perturbation term $\tilde{p}$, such that

$$p(x, t) = p_0(z) + \tilde{p}(x, t) \tag{1}$$

Likewise, the temperature and density fields are decomposed into

$$T(x, t) = T_0(z) + \tilde{T}(x, t), \qquad \rho(x, t) = \rho_0(z) + \tilde{\rho}(x, t) \tag{2}$$

The ambient pressure and density are related through the hydrostatic condition

$$\frac{dp_0}{dz} = -\rho_0 g \tag{3}$$

and the temperature and density perturbations can be related through the equation of state taken in the small disturbance, low-Mach-number form appropriate to this problem:

$$\frac{\rho - \rho_0}{\rho_0} = -\frac{T - T_0}{T_0} \tag{4}$$

The most important consequence of this form of the equations is that the convective derivative of pressure in the energy equation is approximated as $dp_0/dt \approx w\, dp_0/dz$. This simplification and Eq. (4) eliminate acoustic waves from the solution. The prevailing wind is aligned with the positive x axis, and the streamwise diffusion is ignored. The crosswind velocity components (v, w) lie in the y–z plane normal to the direction (x) in which flows the uniform ambient wind U_∞, as is shown in Fig. 1. The simplified equations are 1) conservation of mass (incompressibility):

$$\nabla \cdot u = 0 \tag{5}$$

2) conservation of momentum:

$$\rho_\infty \left[U_\infty \frac{\partial u}{\partial x} + (u \cdot \nabla)u \right] + \nabla \tilde{p} - \tilde{\rho}g = \mu \nabla^2 u \tag{6}$$

and 3) conservation of energy:

$$\rho_\infty c_p \left(U_\infty \frac{\partial \tilde{T}}{\partial x} + u \cdot \nabla \tilde{T} \right) - \left(\frac{dp_0}{dz} - \rho_0 c_p \frac{dT_0}{dz} \right) w = \dot{q} + k \nabla^2 \tilde{T} \tag{7}$$

The eddy viscosity μ and thermal conductivity k are based on the grid spacing. They represent the effects of subgrid-scale mixing in the model. As such, their magnitude is directly related to the spatial resolution employed in the simulations. This role is discussed in more detail in Sec. III.
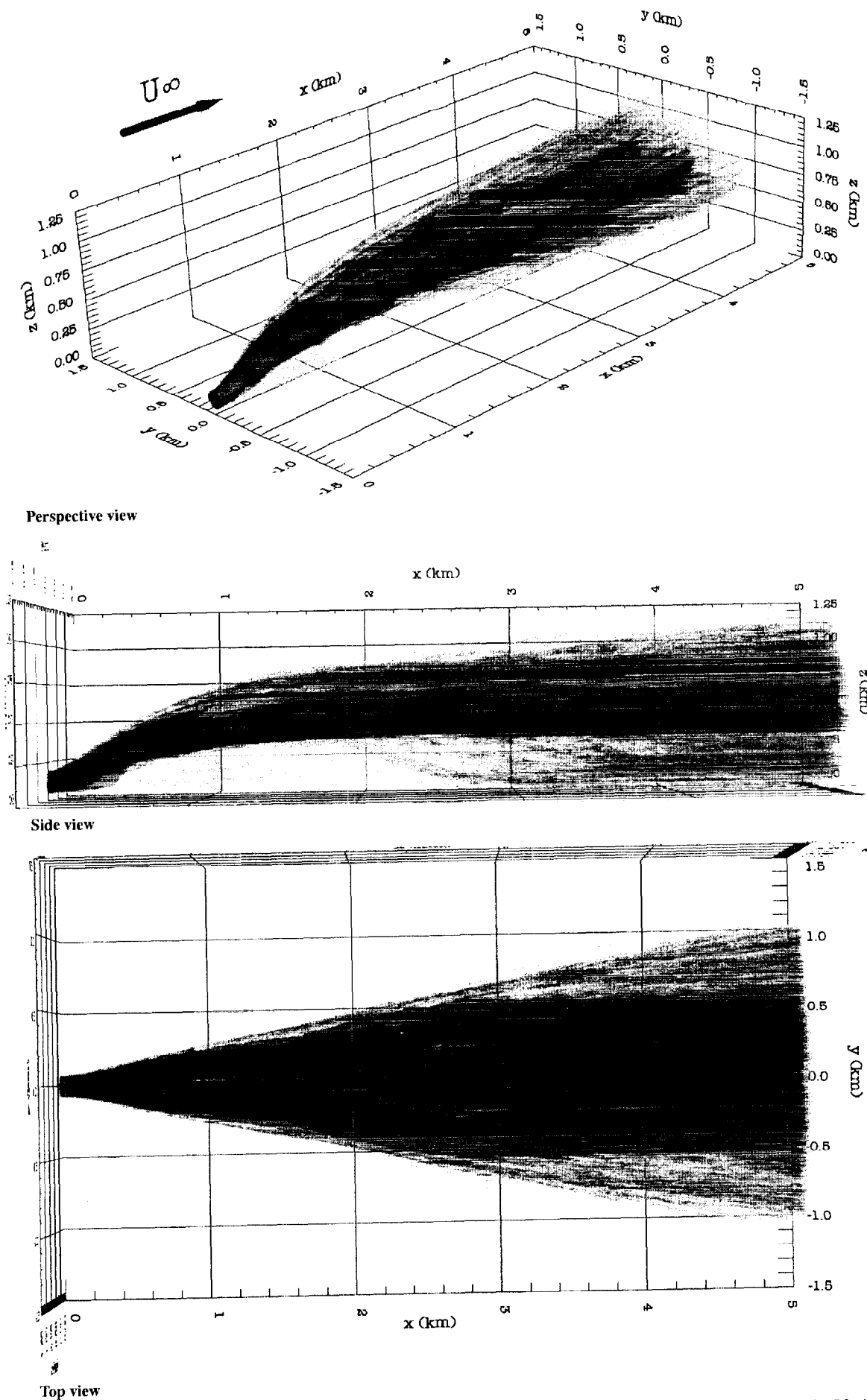
Perspective view

Side view

Top view

Fig. 1   Three views of a single 1-GW fire plume demonstrate the formation and breakup of the counter-rotating vortex pair: $M = 5$ kg/s, $n = 30,000$, $U_\infty = 6$ m/s, $\sigma_\theta = \sigma_{\phi\infty} = 5$ deg. The overlapping surfaces in each view correspond to surfaces of constant concentration with (light, medium, dark) gray = (150, 1000, 5000) μg/m^3.

The required information about the fires is the total convective heat release rate Q, the total particulate mass flow rate M, and the displacements s, which describe the distances between fires. The initial temperature distribution in the plume cross section is assumed to be Gaussian and to satisfy the integral

$$\int_{-\infty}^{\infty} \int_{0}^{\infty} \rho_\infty c_p U_\infty \tilde{T} \, dz \, dy = Q = \sum_{i=1}^{n_f} Q_i \qquad (8)$$

The particulate matter is considered a passive scalar and thus has no effect on the hydrodynamic scaling or calculation. The role played by s is covered in Sec. IV.

The scaling of the governing equations is based on the net strength of the fires, the stratification of the lower atmosphere, and the magnitude of the prevailing wind.[19] The physical length scale in the y–z plane is given by

$$L = \left(\frac{Qg}{c_p T_\infty \rho_\infty U_\infty N_\infty^2} \right)^{\frac{1}{3}} \qquad (9)$$

where L roughly corresponds to the plume rise height. Here, N_∞ is the ground-level value of the Brunt–Väisälä frequency N_0, defined as $N_0^2 = (g/\theta_0)(d\theta_0/dz) = (g/T_0)(dT_0/dz + g/c_p)$. The windward spatial coordinate x is replaced by a pseudotemporal coordinate:

$$t^* = (N_\infty/U_\infty)x \qquad (10)$$

The velocity of the air in the crosswind plane is scaled by

$$V = N_\infty L \qquad (11)$$

The approximations used to generate the simplified parabolic equations can be regarded as the result of a formal asymptotic expansion based on the relative smallness of V/U_∞. A domain of height L would chop off the top half of the plume (because the rise height is an average quantity) and therefore an adjustable scale factor f is used to ensure that the top edges of the plumes are contained within the simulated physical domain. Now the computational length scale fL and velocity scale fV are used to define dimensionless crosswind spatial coordinates (y^*, z^*) and velocities (v^*, w^*) as follows:

$$(y, z) = fL(y^*, z^*), \qquad (v, w) = fV(v^*, w^*) \qquad (12)$$

The nondimensional temperature perturbation $\tilde{T}^*$ and pressure perturbation $\tilde{p}^*$ are defined, respectively, as

$$\tilde{T} = \frac{fQ}{c_p \rho_\infty U_{max} L^2} \tilde{T}^*, \qquad \tilde{p} = \rho_\infty f^2 V^2 \tilde{p}^* \qquad (13)$$

Finally, the turbulent Reynolds and Prandtl numbers are

$$Re = \frac{f^2 \rho_\infty V L}{\mu}, \qquad Pr = \frac{\mu c_p}{k} \qquad (14)$$

The dimensionless form of the conservation laws are now given as 1) conservation of mass (incompressibility):

$$\frac{\partial v^*}{\partial y^*} + \frac{\partial w^*}{\partial z^*} = 0 \qquad (15)$$

2) conservation of momentum:

$$\frac{\partial v^*}{\partial t^*} + v^* \frac{\partial v^*}{\partial y^*} + w^* \frac{\partial v^*}{\partial z^*} + \frac{\partial \tilde{p}^*}{\partial y^*} = \frac{1}{Re} \left(\frac{\partial^2 v^*}{\partial y^{*2}} + \frac{\partial^2 v^*}{\partial z^{*2}} \right) \qquad (16)$$

$$\frac{\partial w^*}{\partial t^*} + v^* \frac{\partial w^*}{\partial y^*} + w^* \frac{\partial w^*}{\partial z^*} + \frac{\partial \tilde{p}^*}{\partial z^*} - \tilde{T}^* = \frac{1}{Re} \left(\frac{\partial^2 w^*}{\partial y^{*2}} + \frac{\partial^2 w^*}{\partial z^{*2}} \right) \qquad (17)$$

and 3) conservation of energy:

$$\frac{\partial \tilde{T}^*}{\partial t^*} + v^* \frac{\partial \tilde{T}^*}{\partial y^*} + w^* \frac{\partial \tilde{T}^*}{\partial z^*} + N^{2*} w^* = \frac{1}{RePr} \left(\frac{\partial^2 \tilde{T}^*}{\partial y^{*2}} + \frac{\partial^2 \tilde{T}^*}{\partial z^{*2}} \right) \qquad (18)$$

subject to the initial conditions

$$v^*(y^*, z^*, t^* = 0) = w^*(y^*, z^*, t^* = 0) = 0 \qquad (19)$$

$$\int \int \tilde{T}^*(y^*, z^*, t^* = 0) \, dy^* \, dz^* = \frac{1}{f^3} \qquad (20)$$

Initially, the crosswind velocity components v and w are assumed to be zero, although this assumption is not restrictive. No-flux, free-slip boundary conditions are prescribed at the ground, consistent with the assumed uniformity of the prevailing wind and the resolution limits of the calculation. The perturbation temperature and pressure have zero normal derivative at the ground and zero value at all other boundaries. The scaling laws display explicitly the dependence of all physical variables on the total fire strength Q and ambient wind speed U_∞ for a given atmospheric stratification and firebed geometry. Thus, computations performed for a fixed value of the parameters can be readily reinterpreted as those quantities are varied. The preceding solutions to the Boussinesq equations are inherently time-averaged.

The smoke transport is calculated by transporting Lagrangian particles through the calculated velocity field. Their locations are distributed onto the computational grid to arrive at a concentration field such as that shown in Fig. 1. As the smoke spreads farther downwind, it goes from a regime governed by fire plume dynamics to one of essentially random atmospheric fluctuations. The trajectories of the Lagrangian particles used to represent the smoke particulate are randomly perturbed from their mean paths to mimic these spatial and temporal fluctuations of the wind and its underlying turbulence. Specifically, the motion of each particle is governed by the mean wind field (u, v, w) plus a perturbation velocity field (u', v', w') that represents the random temporal and spatial variations of the wind. For this study, it is assumed that $u = U_\infty$ and that $u' = 0$. Atmospheric turbulence is described by the measured angles σ_θ and σ_ϕ. A tabular classification of atmospheric turbulence is given by Pasquill.[25] This table may be used to arrive at estimates for σ_θ and σ_ϕ. (Reference 26 contains a discussion of these parameters and methods of evaluating them.) The angles σ_θ and σ_ϕ may be interpreted as averaged over a time period of 10 min to 1 h. They in turn are used to describe the crosswind fluctuations: $\sigma_v = U_\infty \sin(\sigma_\theta)$, $\sigma_w = U_\infty \sin(\sigma_\phi)$. The remaining perturbation velocity components are derived from the following recursive relations[25,27]:

$$v'(t + \delta t) = R_v(\delta t) v'(t) + v'', \qquad w'(t + \delta t) = R_w(\delta t) w'(t) + w'' \qquad (21)$$

$$R_v(\delta t) = e^{-\delta t/\tau_v}, \qquad R_w(\delta t) = e^{-\delta t/\tau_w} \qquad (22)$$

$$v'' = F_N\left(0, \sigma_v \sqrt{1 - R_v^2}\right), \qquad w'' = F_N\left(0, \sigma_w \sqrt{1 - R_w^2}\right) \qquad (23)$$

The double-primed terms are random variables with Gaussian distributions of zero mean whose variances are those of the perturbation velocities' variances multiplied by $(1 - R_v^2)$ and $(1 - R_w^2)$, respectively, ensuring that the variance of each velocity component will not change from one time step to another. The σ_v^2 and σ_w^2 are the variances of v' and w', respectively. The functions R_v and R_w are Lagrangian correlation coefficients taken as exponentials. The parameter τ is indicative of the period of atmospheric fluctuations[28]: $\tau_v = 300$ s and $\tau_w = 100$ s in this study.

Usually, the smoke plume resides mainly in what is referred to as the planetary boundary layer, also called the mixing layer, where the atmosphere is directly influenced by the presence of the Earth's surface. The depth of this layer can vary from roughly 50 m to several thousand meters. Within it, the interaction of the complex terrain, solar heating, and surface friction creates a turbulent wind field, to which the solution of the preceding equations may be considered a time average. The values of the wind fluctuation parameters from Ref. 25 are appropriate within this mixing layer. However, it often happens that the smoke plume, because of the tremendous thermal buoyancy, will penetrate the top of the mixing layer. When this happens, the plume is subject to far less random or turbulent motion. As a result, the magnitude of the vertical wind fluctuations used in the model are reduced from their ground level value $\sigma_{\phi\infty}$ for those particles that penetrate the top of the mixing layer.

III. Numerical Methods

Finite differences on a staggered grid are used to discretize the partial differential equations of motion. A second-order Runge–Kutta scheme with variable step size is used to advance the discretized field variables and to transport the particulate. The solution of a Poisson equation is required to determine the pressure for each Runge–Kutta update to ensure the conservation of mass.

Each plume is introduced as an initial distribution of positive temperature difference and of particles in the y–z plane. As the solution is being marched forward in the x direction, new plumes are introduced when the solution reaches each plume's introductory y–z plane. Note that all of the multiple plume dynamics are a consequence of the numerical solution of the governing equations. No changes were made to the model equations, and no superposition of single-plume solutions is used.

The energy equation is initialized by prescribing the perturbation temperature profile in the y–z plane a few fire diameters downwind of each fire. In the absence of measured input data, a Gaussian profile just downwind of each fire can be used subject to the condition that

$$\sum_{j=1}^{J}\sum_{k=1}^{K} \bar{T}_{jk}^{*0}\delta y^*\delta z^* = \frac{1}{f^3} \qquad (24)$$

Numerical studies confirm that the downwind dispersion pattern is not very sensitive to the choice of these initial parameters. The width of each initial plume cross section can be taken to be roughly that of the corresponding fire. The boundary conditions for the perturbation temperature are adiabatic at the ground and zero at the other three edges of the computational domain.

To facilitate the numerical solution of the equations, the momentum equations are rewritten as

$$\frac{\partial v^*}{\partial t^*} - w^*\omega + \frac{\partial \mathcal{H}^*}{\partial y^*} = -\frac{1}{Re}\frac{\partial \omega}{\partial z^*}$$

$$\frac{\partial w^*}{\partial t^*} + v^*\omega + \frac{\partial \mathcal{H}^*}{\partial z^*} - \bar{T}^* = \frac{1}{Re}\frac{\partial \omega}{\partial y^*}$$

The term $|u^*|^2/2$ has been combined with the perturbation pressure $\bar{p}^*$ to form a total head $\mathcal{H}^* = |u^*|^2/2 + \bar{p}^*$. The vorticity vector $\omega = \nabla \times u$ reduces to a scalar $\omega \equiv \omega_x$ because of the uniform flow in the downwind x direction. Free-slip conditions are prescribed for the tangential component of the velocity at all boundaries, consistent with the uniform wind assumption and spatial resolution of the grid. The boundary condition for the normal component of velocity is associated with the boundary condition for the pressure and is described in the next section. The initial velocity field is zero.

This model is a large eddy simulation (LES) with a simple subgrid model. For LES, the effect of turbulence from structures smaller than the finest numerical grid resolution must be modeled, usually in the form of an expression for the eddy viscosity μ. In this work, the simplest possible model $\mu \propto (\delta z^*)^2$ is used. This is consistent with more involved expressions[29] for μ and ensures that the Reynolds number based on the eddy viscosity is proportional to the number of grid cells in each crossflow plane. Thus, the ratio of maximum to minimum resolved length scales is proportional to $Re^{1/2}$, in accordance with the mathematical structure of the two-dimensional, time-dependent, Navier–Stokes equations. The spirit of this approach is to emphasize high spatial resolution instead of advances in subgrid modeling.

The variable time step δt^* is based on the Courant–Friedrichs–Lewy (CFL) condition

$$0 < \max_{ij}\left\{\delta t^*\left\|\left(v_{ij}^*/\delta y^*, w_{ij}^*/\delta z^*\right)\right\|_1\right\} < \varepsilon_{CFL} < 1 \qquad (25)$$

where ε_{CFL} is a tolerance chosen by the user. This condition guarantees that a particle in the flow cannot travel more than the width of a grid cell in a single time step.

Before the velocity components can be updated, it is necessary to determine the gradient of the total head. Taking the divergence of the momentum equations in the vector-invariant form

$$\frac{\partial u^*}{\partial t^*} + F^* + \nabla \mathcal{H}^* = 0 \qquad (26)$$

where F^* denotes the nonlinear convection, buoyancy, and dissipative terms, yields a Poisson equation for the total head:

$$\nabla^2 \mathcal{H}^* = -\nabla \cdot F^* \qquad (27)$$

The incompressibility condition [Eq. (5)] eliminates the pseudo-time derivative of the velocity because the divergence is zero. In discretized form, this Poisson equation for the total head is solved with a very efficient direct Poisson solver that exploits the uniform gridding of the computational domain through the use of fast Fourier transforms.[30] The boundary conditions for this elliptic equation are mixed. At the ground, the vertical component of velocity w^* is zero. At the top and side boundaries, the pressure is assumed to be at its ambient value; thus the perturbation pressure is assumed to be zero. Applying the steady-state form of Bernoulli's theorem, the total head $\mathcal{H}^*$ does not change along streamlines. Thus, for outgoing flow, $\mathcal{H}^* = |u^*|^2/2$, and for incoming flow, $\mathcal{H}^* = 0$.

As the velocity field evolves in the crosswind plane, the trajectories of the Lagrangian particles that are used to represent the particulate matter are computed. The particles are introduced into the flow at the start of the calculation and advected with the induced flow, given by the velocity field $(U, v + v', w + w')$. The particulate distribution is initialized as a random distribution of n_i particles for the ith plume contained within an ellipse of semiaxes $(\beta_{y_i}, \beta_{z_i})$, satisfying the integral

$$\int_{-\infty}^{\infty}\int_{0}^{\infty} \rho_p U_\infty \, dz \, dy = M = \sum_{i=1}^{n_f} M_i \qquad (28)$$

The number of particles originating from the ith plume is $n_i = n_p M_i/M$. The quantity ρ_p is nondimensionalized:

$$\rho_p = (fM/UL^2)\rho_p^* \qquad (29)$$

so that Eq. (28) is now nondimensionalized such that

$$\sum_{j=1}^{J}\sum_{k=1}^{K} \rho_{p,jk}^*\delta y^*\delta z^* = \frac{1}{f^3} \qquad (30)$$

The total mass delivered to any cell is given by the summation of the masses of all particles that pass within one cell width of the center of said cell. The particulate density of jkth cell may be expressed as the sum of the contributions of all particles in its neighborhood such that

$$\rho_{p,jk}^* = \sum(1 - r_{y^*})(1 - r_{z^*})\frac{1/f^3}{n\delta y^*\delta z^*} \qquad (31)$$

where n is the total number of particles representing the plume cross section and r_{y^*} and r_{z^*} are the lateral and vertical distances from the cell center, expressed as fractions of the cell dimensions.

Numerical experiments are carried out to quantify the errors and costs associated with this method. For these experiments, a single 500-MW fire producing smoke at 2.5 kg/s is used. Fifteen thousand Lagrangian particles are used to track the smoke trajectory. The initial particle distribution in the y–z plane is circular with a diameter of 80 m, the atmosphere is linearly stratified at $-5°$C, $f = 5$, and the prevailing ambient wind is 6 m/s. The atmospheric dispersion angles are zero in both the y and the z directions.

At each computational x location, the perturbation temperature $\tilde{T}$ is integrated across the half-plane $\{[y_{min}, 0], [0, z_{max}]\}$ and is then divided by the area of the half-plane. The same is done for the first two temperature moments, $y_{\tilde{T}^*}^*$ and $z_{\tilde{T}^*}^*$. The results are shown in Fig. 2 for successively refined grids. At each successive grid refinement, the Reynolds number is quadrupled. Richardson extrapolation is applied to the two most refined grids. This final curve represents the best estimate of the continuous solution to the model equations as $Re \to \infty$. Note that convergence only has meaning for some kind of averaged quantities, of which those displayed here are but three of the many possibilities. Pointwise convergence for such highly unstable flows is probably a fruitless pursuit because the refinement exercise will resolve more and more of the fine eddy structure.

The preceding calculations were done in double precision and proceeded up to $x = 5.9$ km (i.e., $x^* = 5$). The 512 × 256 resolution case had $Re = 8 \times 10^4$ and required 798 steps and 17.5 MB

Half-plane total temperature

z-temperature moment

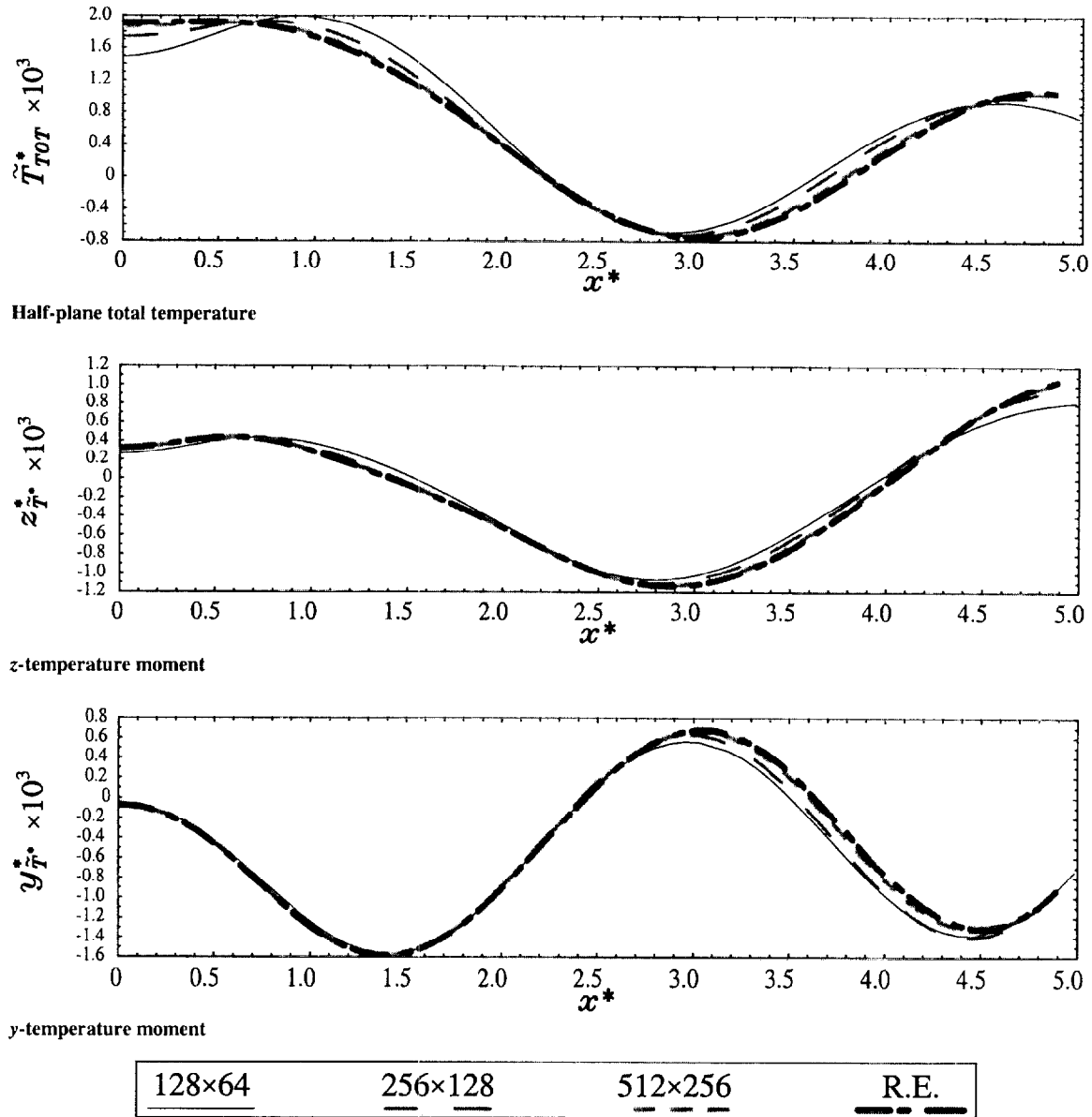y-temperature moment

| 128×64 | 256×128 | 512×256 | R.E. |

Fig. 2   Integrated perturbation temperature and the y and z moments demonstrate convergence as the computational grid is refined. The curve labeled "R.E." is derived by performing Richardson extrapolation on the two most refined curves.

of memory to run to completion in 13 min on an SGI workstation with the R10000 CPU. For 256×128, $Re = 2 \times 10^4$, 330 steps were taken and 9.7 MB were used in 1.9 min on the same hardware. For the coarsest case of 128×64, which had $Re = 5 \times 10^3$, 149 steps were taken and 6.1 MB were used in 0.49 min. Validations for this approach were published in Ref. 19.

The parabolic approximation makes this model ideal for predicting concentrations far downwind of the fire. The counter-rotating vortex pair, which causes the plume to rise and has a pronounced effect on particulate concentration profiles, is resolved by this approach, and it is the dominant fluid mechanical feature [O(1 km)] downwind of the fire.

The present approach allows for high resolution in each y–z plane. It only resolves one component of vorticity in the x direction. However, because the solution evolves in the x direction, so does the x component of vorticity. This is sufficient to allow the plumes to spread and to allow each plume's vorticity profiles to interact with that of others in close enough proximity.

A demonstration of this model's capabilities follows. A single plume is presented that will serve as the prototype for the dual-plume simulations covered in the next section. It is generated by a 1-GW fire producing smoke at 5 kg/s. The concentration field is represented by 30,000 Lagrangian particles. The initial particle dis-

tribution in the y–z plane is circular with a diameter of 120 m, the atmosphere is linearly stratified at $-5°C$, $f = 4$, and the prevailing ambient wind is 6 m/s. The atmospheric dispersion angle is a constant 5 deg in the y direction and in the vertical $\sigma_{\phi\infty} = 5$ deg. Three views of this single fire plume are given in Fig. 1. Surfaces of constant concentration, which are the three-dimensional analogs of contours, highlight three different concentration values. The outermost value, $\rho_p = 150 \, \mu g/m^3$, corresponds with the maximum safe limit of smoke concentration. It is denoted in light gray. The other two concentration levels, 1000 and 5000 $\mu g/m^3$, were chosen so as to reveal internal plume structures. The resolution for this calculation in the y–z plane is 512×128 points, or 65,536 cells. This gives a little less than a 10-m resolution limit in the y and z directions. As was explained in Sec. III, the updated positions of each Lagrangian particle are distributed onto the grid to resolve the concentration field. Figure 1 conveys the complete resolution of the numerical calculation. Comparing the interior of the plume with the boundary illustrates how increasing the number of particles provides a smoother, i.e., less streaky, concentration field.

Physically, a counter-rotating vortex pair is formed that lofts the plume up to a stable altitude and corrals most of the particulate into two tubes. Once the plume reaches a stable altitude, attempts by the vortices to move denser air to higher altitudes (of lower density
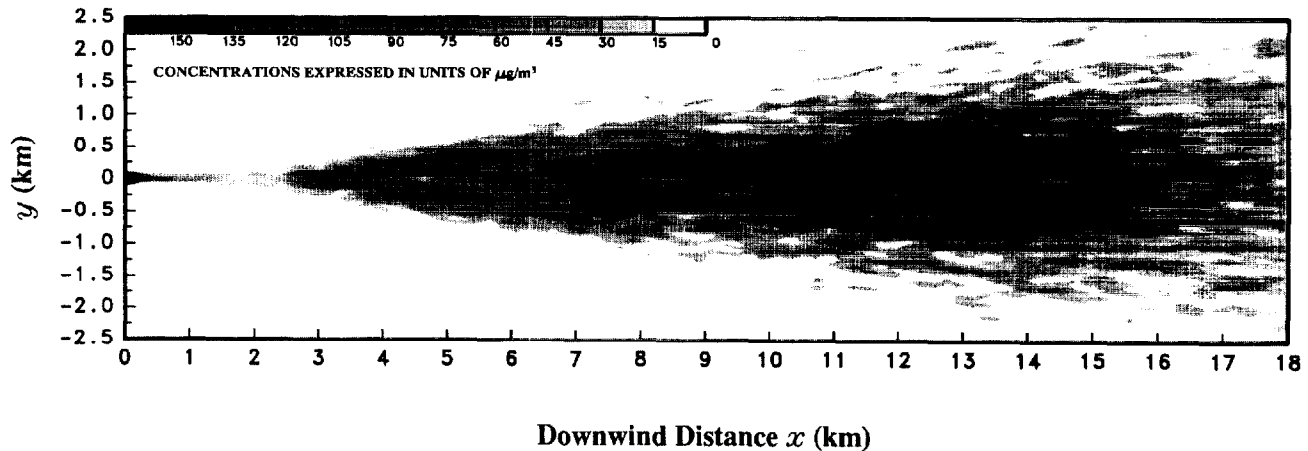
Fig. 3 Ground-level concentration yielded by 30,000 particles from a 1-GW plume emitting at 5 kg/s passing through a ±5-deg disturbed atmosphere produces substantial ground-level deposition that begins to drop off after $x = 15$ km.
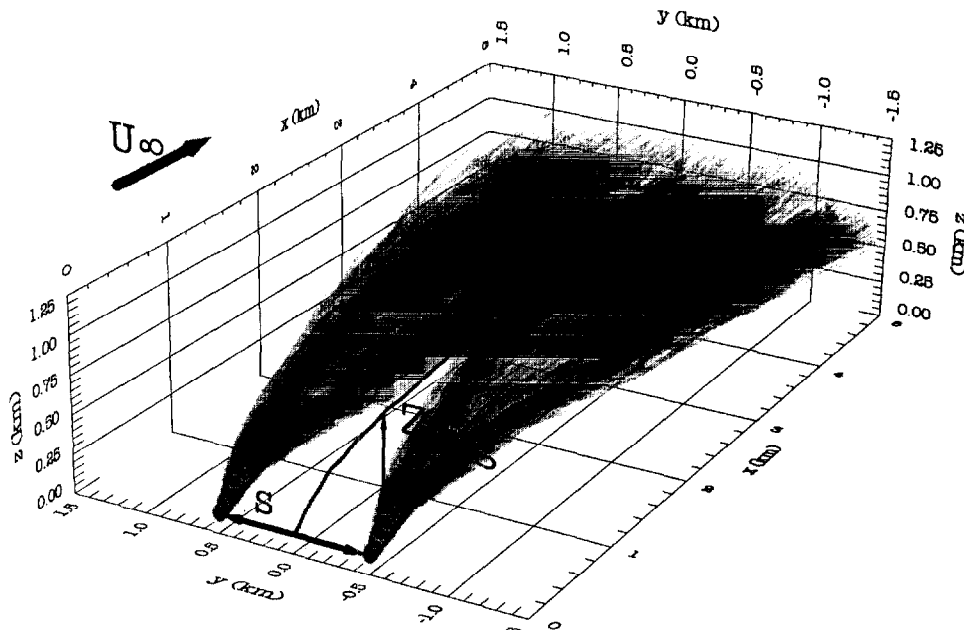

Fig. 4 Average height profile Z_{avg} stays exactly in between the two plumes because $s_x = 0$: $s_y = 1$ km, $Q_i = 500$ MW, $M_i = 2.5$ kg/s, $n_i = 15{,}000$, $U_\infty = 6$ m/s, $\sigma_\theta = \sigma_{\phi\infty} = 5$ deg, (light, medium, dark) gray = (150, 1000, 5000) μg/m^3.

fluid) are countered by negative buoyancy forces. The effect is the same as before but in reverse: when the denser fluid packets move up into less dense strata, vorticity of the opposite sense is formed, slowly killing off the effects of the counter-rotating vortex pair. As the zones of vorticity concentration are dispersing, the background wind fluctuations begins to dominate the flow. This not only releases particulate from the confines of the high density tubes but it also brings particulate to the ground. The ground-level deposition is shown in Fig. 3. Comparisons of ground-level deposition predictions with large-scale experiments can be found in Ref. 19.

IV. Two-Plume Interactions

One of the great temptations in multiple-plume analysis is to treat such a scenario as a superposition of single plumes. Closely tied to this is the concept of independence. Plumes are usually considered to be independent if their fluid and thermal fields essentially do not overlap. Plumes not satisfying this criterion are usually lumped into a larger, superplume that is otherwise indistinguishable from a single plume. Although independent plumes do behave like two single plumes, two interacting plumes have marked differences from a lumped single plume.

Unless otherwise stated, each individual plume shown in this paper will be the consequence of a 500-MW fire producing smoke at 2.5 kg/s. Each plume's smoke concentration field is represented by

15,000 Lagrangian particles. To avoid having the plethora of possible input parameters obscure the fire plume dynamics, the following simplifications are imposed: The initial particle distribution in the y–z plane is circular with a diameter of 60 m, the atmosphere is linearly stratified at -5°C, $f = 4.25$, and the prevailing ambient wind is 6 m/s. The wind fluctuations are a constant 5 deg in the y direction, and in the vertical $\sigma_{\phi\infty} = 5$ deg.

A quantitative analysis of two interacting plumes is presented in this section. The particles are used to derive three important metrics for quantifying plume dispersal. The average height is described as
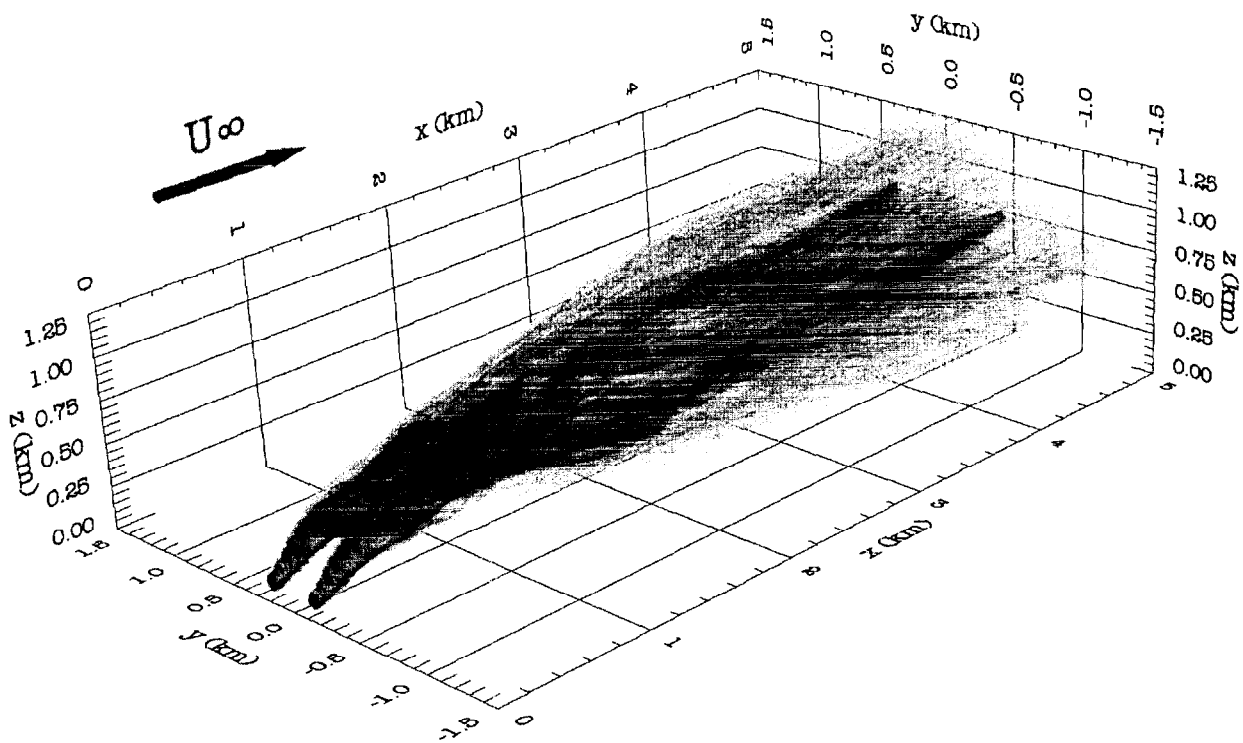
$$Z_{avg}(x) = \sum_{i=1}^{n} Z_{p,i}(x)/n \tag{32}$$

where $Z_{p,i}$ is the height of the ith particle at x. The Z_{avg} is analogous to the plume rise for a single plume or the averaged plume rise of multiple plumes. The spread in the two crosswind coordinates are
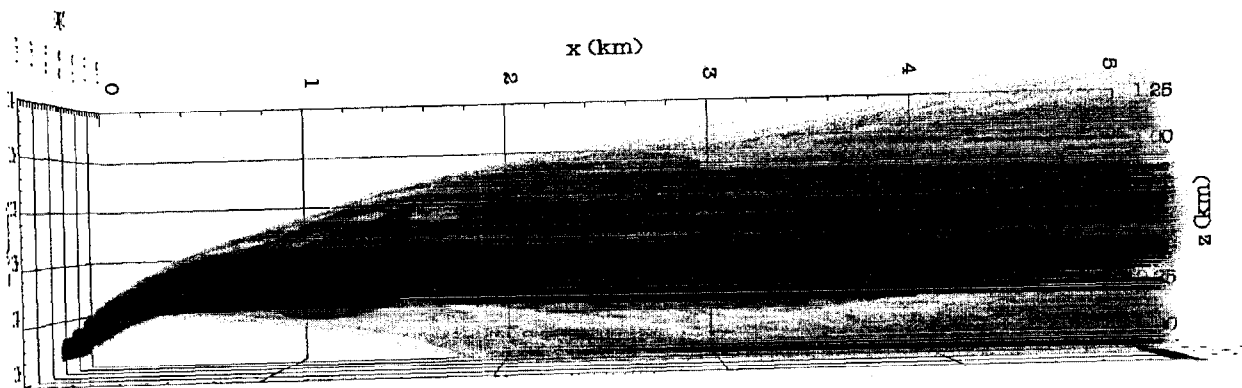
$$\sigma_y(x) = \sqrt{\sum_{i=1}^{n} [Y_{p,i}(x) - Y_{avg}(x)]^2/n} \tag{33}$$

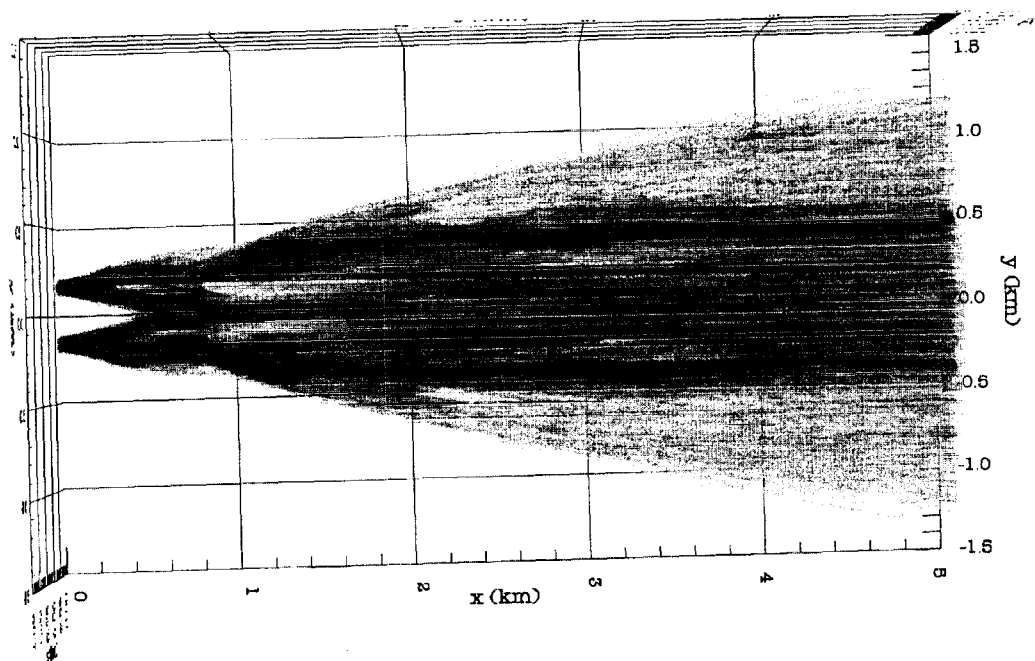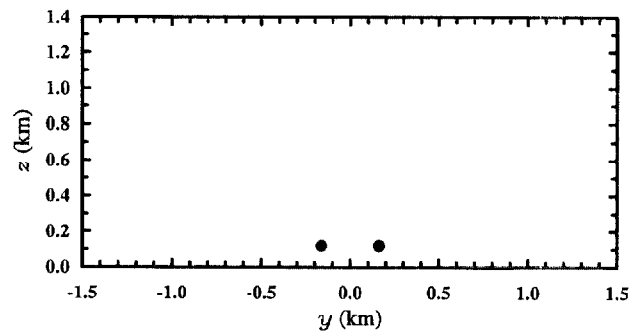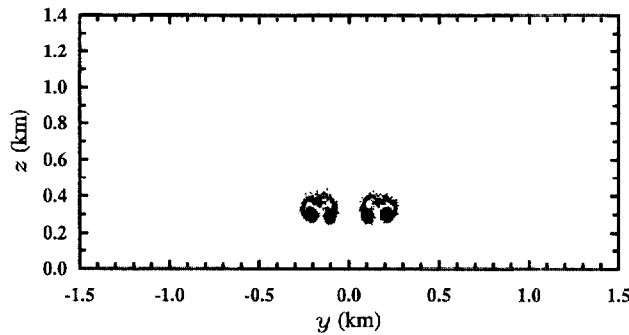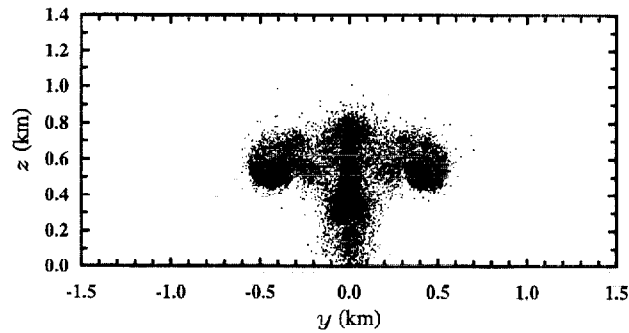$$\sigma_z(x) = \sqrt{\sum_{i=1}^{n} [Z_{p,i}(x) - Z_{avg}(x)]^2/n} \tag{34}$$

Perspective view

Side view

Top view

Fig. 5   Three views of two fire plumes started 325 m apart in the y–z plane yielded a max(Z_{avg}) of 0.55 km under calm conditions ($\sigma_\theta = \sigma_{\phi\infty} = 0$). The results shown here are for $\sigma_\theta = \sigma_{\phi\infty} = \pm 5$ deg, $Q_i = 500$ MW, $M_i = 2.5$ kg/s, $n_i = 15{,}000$, $U_\infty = 6$ m/s, and $f = 4.35$.

a) $x = 0$

b) $x = 350$ m

c) $x = 1900$ m
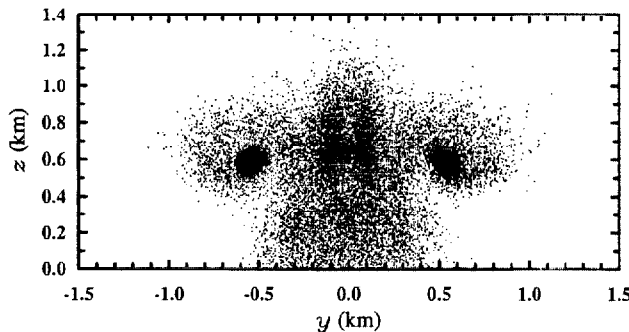
d) $x = 3400$ m

Fig. 6 Four cross sections at $x = (0, 350, 1900, 3400)$ m of the Lagrangian particle locations for the two fire plumes shown in Fig. 5, where the particles of the left plume are colored gray and those of the right black, demonstrate how the interaction of the two inner vortices coupled with the dispersion provided by the atmosphere lead to dense, well-mixed concentration levels above the x axis that cover an area in the y–z plane of about 1 km² at $x = 3.4$ km.

The two components of the plume separation vector s serve as the independent variables for the first parametric study, whereas the suprema of the metrics defined in Eqs. (32–34) are used to describe the effects of the interactions. As shown in Fig. 4, two plumes will be situated at different s displacements in the x–y plane and quantities such as $\max(Z_{avg})$ are recorded for each configuration. Based on an extensive search through the (Q_1, Q_2, s_x, s_y) parameter space resulting from 1080 runs, initial configurations are chosen that demonstrate some of the more dramatic aspects of dual plume interactions. Two plumes are started side by side ($s_x = 0$)
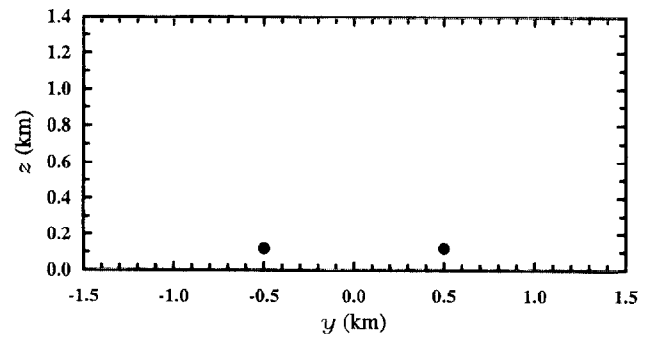
a) $x = 0$
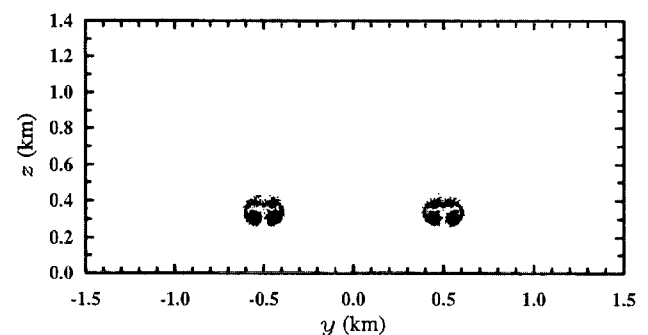
b) $x = 350$ m
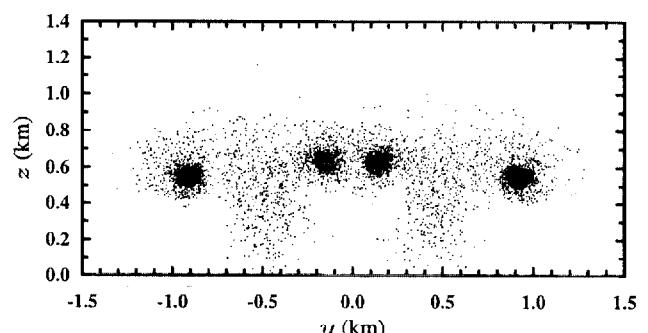
c) $x = 2900$ m
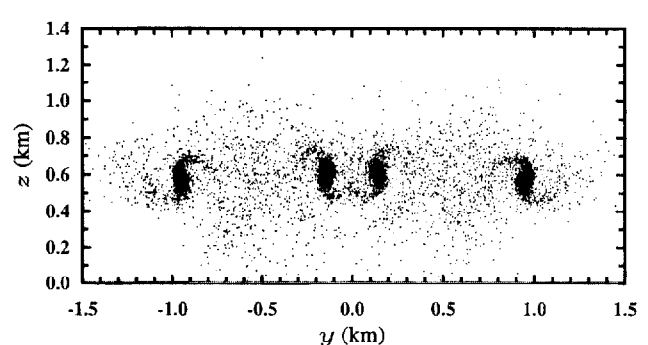
d) $x = 3900$ m

Fig. 7 Four cross sections at $x = (0, 350, 2900, 3900)$ m of the Lagrangian particle locations show that two fire plumes started 1 km apart in the y–z plane interact weakly once the inner concentration cores make contact because each plume has reached a stable height and their vorticity fields are on the wane.

with a separation of $s_y = 325$ m at the same altitude of 120 m with all other parameters as defined in the preceding paragraph. In this setup, the destructive vortex interactions of the two inner structures yielded the lowest $\max(Z_{avg}) = 0.55$ km of any side-by-side case for a calm atmosphere. Randomly perturbing the particles leads to $\max(Z_{avg}) = 0.79$ km. The present configuration is still of interest because the low plume rise was caused by the interaction of the vortices arising from the deterministic calculation. Comparing the side view in Fig. 1 with that in Fig. 5 shows that the atmospheric disturbances were able to disperse particulate that was freed by the contact of the inner smoke concentrations, raising the plume edge
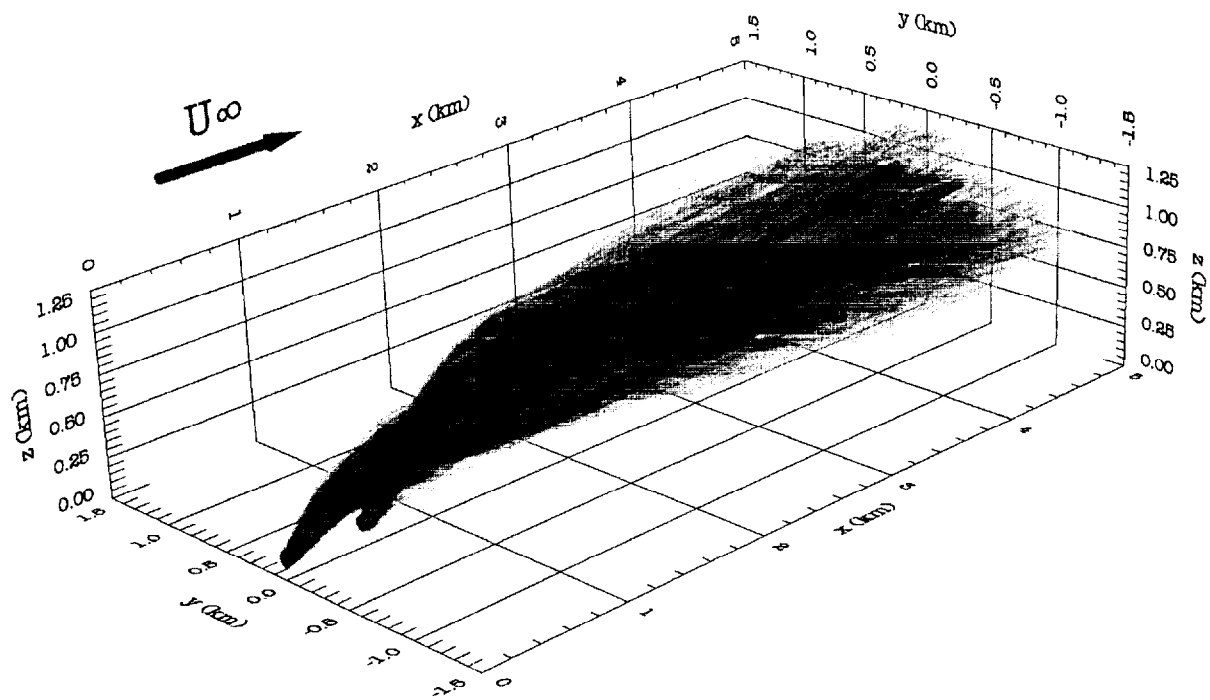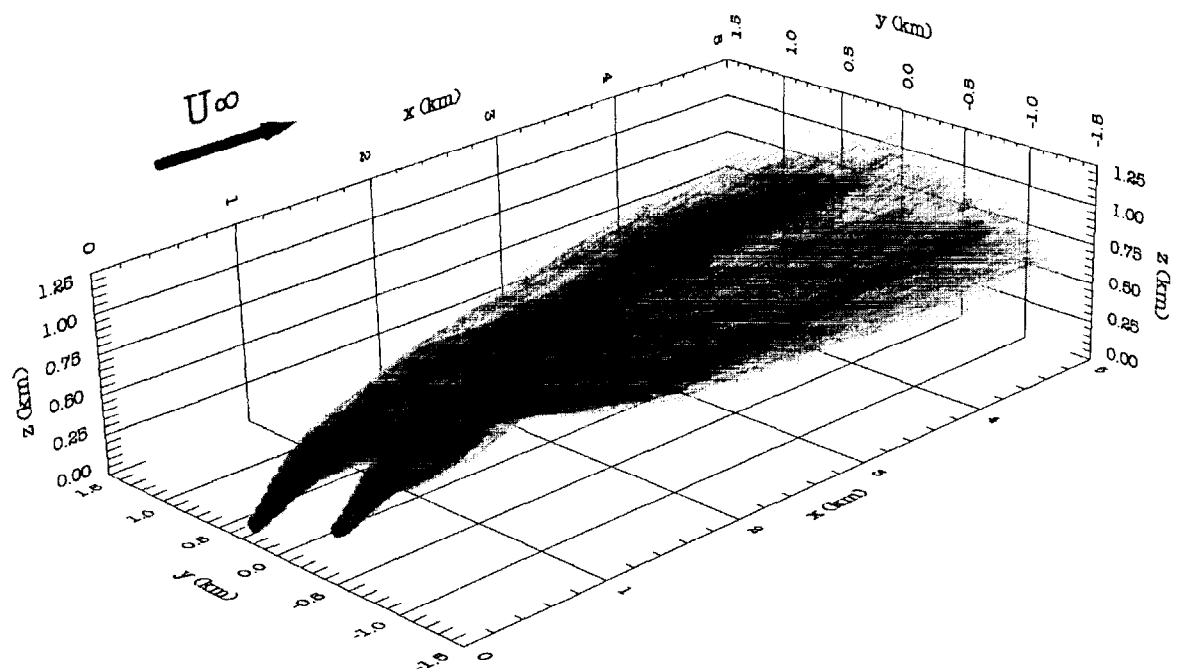
Perspective view
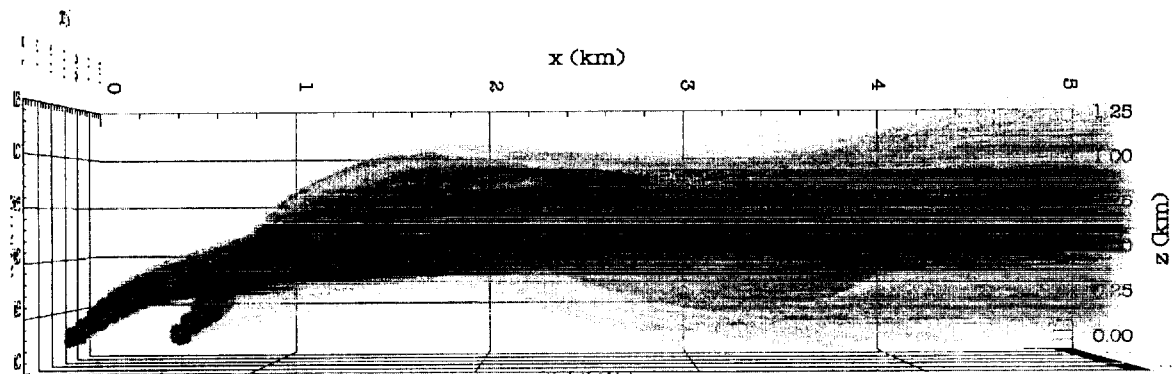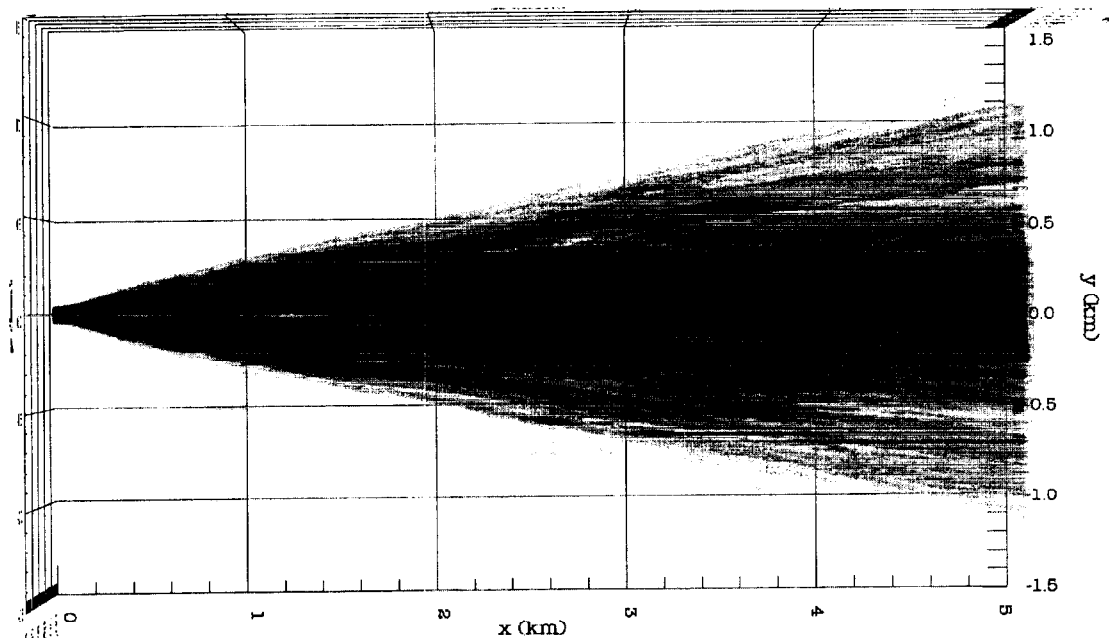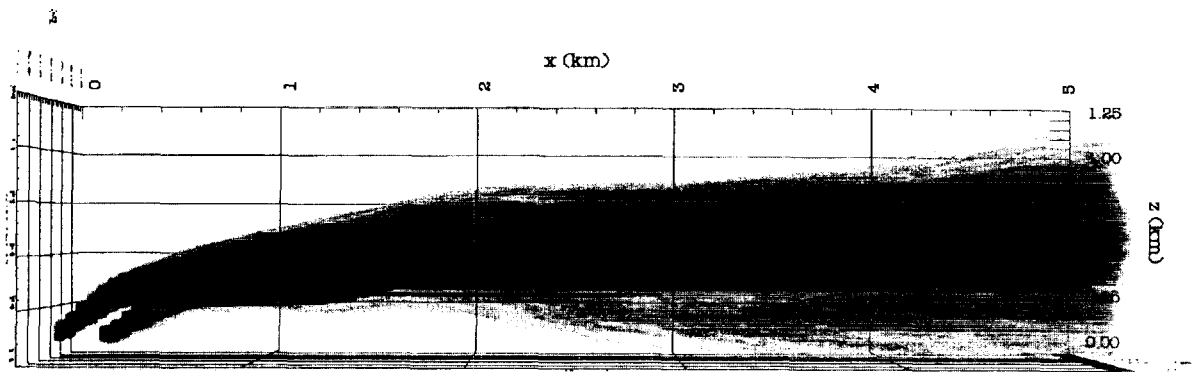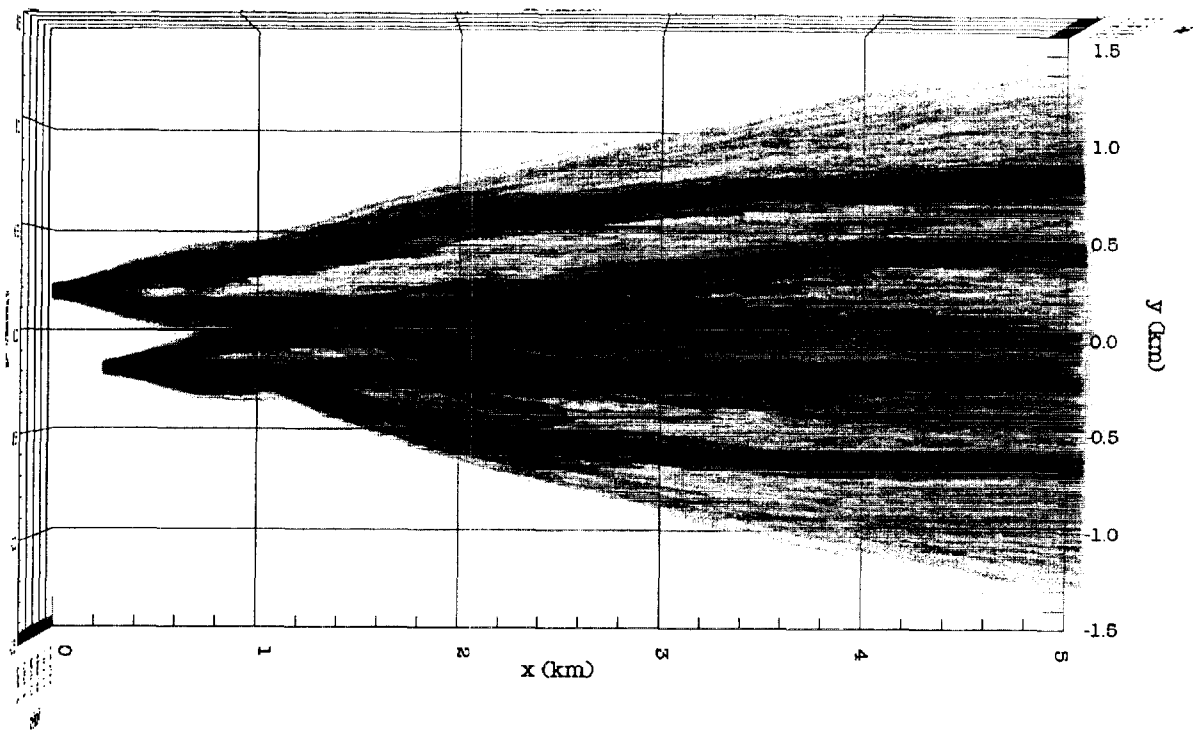

Side view

Top view

Fig. 8 Three views of two 500-MW fire plumes started 500 m apart in the x–z plane demonstrate how the additive interaction of vortices leads to increased plume rise.

Perspective view

Side view

Top view

Fig. 9   Starting two plumes at $(x, y) = (0, -0.19)$ and $(0.28, 0.19)$ km breaks some of the symmetries evident in the preceding examples.

beyond the level attained by one plume. The top view in Fig. 5 shows that, as a consequence of the interaction of the two inner smoke cores, there is a new entity that was absent from the single-plume case; there is a new region of high concentration directly above the x axis. The utility of graphical visualization of surfaces of constant concentration is that interior plume structures can be resolved that in actuality would be obscured by the plume edge, i.e., the $\rho_p = 0$ surface. Judging by the outward appearance only, the only possible conclusion is that the two plumes have combined into a single plume identical to its parents. The inner structure revealed by the surfaces of constant concentration demonstrates that this is not the case. To elucidate this point further, four slices at different x planes are shown in Fig. 6. At $x = 350$ m it can be seen that the two outer vortices are causing the inner ones to rise to higher heights. This mechanism accounts for the increased concentration levels at altitudes higher than those produced by a single plume. By $x = 1900$ m, the plumes have reached a stable rise height and the particulate is being dispersed by atmospheric mixing. The slice for $x = 3400$ m once again shows how atmospheric mixing can, among other things, cause particles to mix out of the plume. These plumes are interdependent.

If the same two plumes are started 1 km apart in the y direction, as is shown in Fig. 4, minimal vortex interaction occurs in the $y-z$ plane. As the cross sections in Fig. 7 demonstrate, the distant vortex pairs exert modest influence on the particles. From the point of view of vortex dynamics, these two plumes are independent. The potential field is responsible for the tilting of each plume pair shown in Fig. 7c because the potential field, which asymptotically behaves like the potential kernel, decays less rapidly than the rotational field (which is asymptotic to the heat kernel). The greater separation provides for overall lower concentrations throughout the domain occupied by the two plumes. Once the two profiles touch, a region of denser particulate concentration forms above the x axis, yielding sizeable tracts of smoke cover. Figure 4 also shows that, because of the substantial separation of the fires, greater area is covered downwind by the twin plumes once their edges meet.

If instead the two plumes are initialized in the $x-z$ plane, then a different set of consequences occur. For this example, two plumes are started in line with a separation of 500 m with all other parameters as defined before. This configuration achieved the highest max(Z_{avg}) with and without atmospheric dispersion. The top view in Fig. 8 shows that, at this proximity, the second plume entrains the first, producing two regions of high particulate concentration. This is a fine example of plume merging, where the resulting plume bears all of the characteristics of the individual plume. Their proximity and alignment also allow the plume farthest downwind to augment the overall plume rise height, pushing substantial quantities of smoke beyond the height of 1 km.

Although the preceding examples help to introduce some of the features of multiple-plume dynamics, the symmetric alignments used to obtain them are rarely evident in the field. If two plumes are started at $(x, y) = (0, -0.19)$ and $(0.28, 0.19)$ km, such as is shown in Fig. 9, a combination of the effects evidenced in the preceding sections is evident. This layout was chosen because it yielded the lowest max(Z_{avg}) under calm conditions ($\sigma_\theta = \sigma_{\phi\infty} = 0$). Concentrations along the y-normal plane where the two plumes first touch are still augmented but, because the circulation in the left plume is stronger at the time of contact, particulate from the right plume gets swirled into the interior of the left plume. This outcome is a mixture of the swirling about vortex cores seen in the $s_y = 0$ case (Fig. 8) with the intersection of inner concentration structures characteristic of an $s_x = 0$ case (Fig. 5). Generalizations or extrapolations based on plumes started in planes that are normal or orthogonal to the prevailing wind direction can at best yield a limited, if somewhat still useful, understanding of interactions between plumes in arbitrary arrangements. These guides become increasingly fallible as the number of plumes is increased, as is demonstrated in the next section.

V. Multiple-Plume Scenarios

Changing the problem to three plumes with a symmetric triangular initial layout such that $(x, y) = (100, 0)$, $(0, -300)$, and $(0,
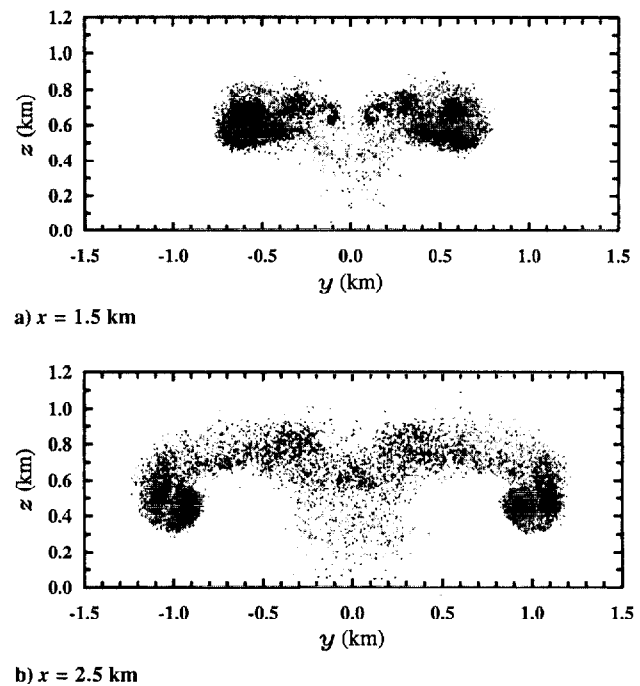

a) $x = 1.5$ km

b) $x = 2.5$ km

Fig. 10 Particulate distribution for three fire plumes started at $(x, y) = (100, 0)$, $(-300, 50)$, and $(300, 50)$ m demonstrates how vortex interactions can radically rearrange the smoke concentration field. The medium-gray particles, which correspond to $(x, y) = (100, 0)$, end up concentrated near the edges of the multiple-plume distribution.

300) m can yield consequences dissimilar from those encountered in the two-plume examples. In Fig. 10a, the center plume has been entrained by the two outer plumes, leaving the area above the x axis with low concentrations. The shearing occurring from these vortex interactions flattens the particulate from the center plume. By $x = 2.5$ km (Fig. 10b), the shearing and entrainment has brought the material from the center plume to the outer edges of the plume conglomeration and the process of mixing because of swirling is underway. The distinction that what was originally in the middle is now located near the outer edges of two outer plumes may not matter much if the three plumes contained the same type of smoke. However, if the particulate in the center is of a different composition than that in the wings, the assumption that the material in the middle would stay in the middle is incorrect. Decisions based on this presumption could lead to unexpected surprises. Furthermore, if the lateral distance between the two side plumes is increased to 700 m, the vortex interactions are just right to produce two strong side-jets that travel out the sides of the domain shown in Fig. 10. It is hard to imagine how an algorithm based on applying the particulate-positioning characteristics of dual plumes three times could produce any of these results.

Mass fire scenarios again further confound the situation. Eight plumes with no initial ground-level symmetry produce a complex set of results (Fig. 11). The cover produced by these plumes casts a shadow over a significant amount of land and it also holds the prospect of dispersing the smoke over a greater area than would be covered by one massive plume of strength Q and mass flow rate M. The vorticity fields responsible for all these dynamics (Fig. 12) display correspondingly involved vortex interaction. With these results, it is not difficult to fathom the source of the unpredictability exhibited by conflagrations. Although the location of particles is indicative of regions of nonzero vorticity, usually the space covered by the particles does not closely correspond with the domain of appreciable vorticity, i.e., the particle boundary is strictly not congruent with the vortex core in these instances. Regions of strong vorticity can successfully confine the smoke. As the particulate proceeds downwind, the diminished fire-induced vorticity can no longer contain the smoke. Here, for all intents and purposes, the fires' influences are no longer felt; the dynamics are now solely governed by the atmosphere.
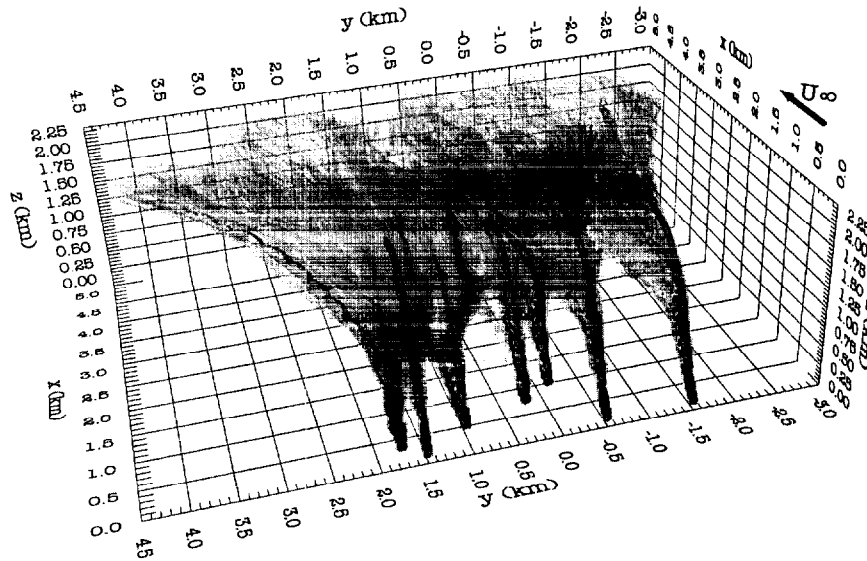
Fig. 11   Surfaces of constant concentration for eight 500-MW fire plumes demonstrate the complexity resulting from multiple-plume interactions; $M_i = 2.5$ kg/s, $n_i = 5000$, $U_\infty = 6$ m/s, $\sigma_\theta = \sigma_{\phi\infty} = 5$ deg, (light, medium, dark) gray = (150, 1000, 5000) μg/m^3. These eight plumes are spread over an area substantially larger than the 10 km^2 covered by a single 4-GW fire plume.
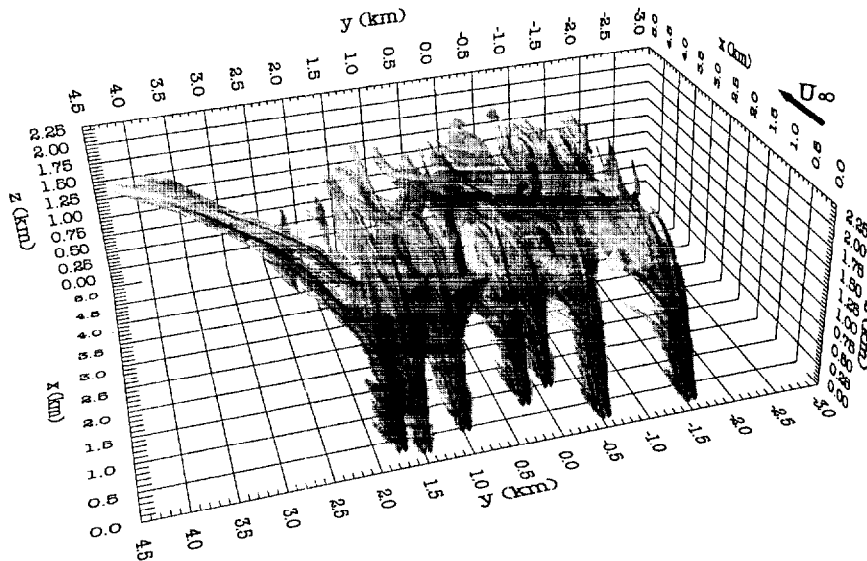

Fig. 12   Interactions of the streamwise vorticity fields for the eight plumes shown in Fig. 11 account for the complex dynamics. Here the light-gray surface corresponds with $\omega = \pm0.05$ Hz, and medium gray corresponds with $\omega = \pm0.15$ Hz.

VI.   Conclusion

Traditional approaches to determining multiple-plume concentrations apply superposition of known particulate distributions, usually Gaussian functions. The results presented here indicate that the fluid mechanics strongly influences the smoke distribution. Because multiple plume interactions are nonlinear, the distribution for particulate from any single plume in a multiplume scenario can differ substantially from that of just one plume. Hence superposition based on a standard distribution seems inappropriate.

Buoyancy creates the vorticity that causes the plume rise. Once density equilibrium has been achieved, the action of vortices to move denser fluid into less dense layers produces the reverse result, eventually eliminating the vorticity. This vorticity destruction process alone spreads the particulate horizontally at the stable plume rise height. Hence, the particulate distribution is not indicative of regions of high vorticity for the whole range of the problem. The best correlation between the two occurs while the vortex strengths are increasing. This correspondence decreases once the point of maximum buoyancy-induced vortex strength is passed. Once the vortex strengths begin to die down, the process of atmospheric dispersion dominates the flow. Atmospheric dispersion on its own can spread the smoke downwind. It, however, cannot cause the smoke

to rise uniformly to a stable altitude. The plume rise is clearly the effect of the buoyancy. However, background atmospheric motion can mix particulate to the ground, making it an important agent in ground-level smoke deposition.

Multiple-fire-plume interactions can move particulate to unexpected places downwind, making the straightforward extrapolation of the elements of any particular individual plume based on its initial position an inaccurate proposition. It has been demonstrated that multiple-plume interactions can push particulate up to altitudes exceeding any single constituent plume's capability. Once the vorticity diminishes, the atmosphere can produce well-mixed smoke distributions more in tune with the predictions of classic plume models. However, the number of plumes and their initial locations control the downwind distance required to achieve this state. This means that for possibly several kilometers, the smoke concentration field will have structures that may be to the advantage or disadvantage of those in this vicinity.

References

[1]Raloff, J., "Burning Issues," *Science News*, Vol. 144, Oct. 1993, pp. 220–223.

[2]Trelles, J., "Mass Fire Modeling of the 20 October 1991 Oakland Hills Fire," Ph.D. Dissertation, Mechanical Engineering Dept., Univ. of California, Berkeley, CA, 1995.

[3]Anfossi, D., Bonino, G., Bossa, F., and Richiardone, R., "Plume Rise from Multiple Sources: A New Model," Atmospheric Environment, Vol. 12, No. 9, 1978, pp. 1821–1826.

[4]Anfossi, D., Richiardone, R., and Bonino, G., "An Application of a Plume Rise Model for Multiple Sources to the Cooling Tower Plumes of John E. Amos Power Plant," Il Nuovo Cimento, Vol. 2C, No. 4, 1979, pp. 488–497.

[5]Anfossi, D., Alessio, S., and Briatore, L., "Laboratory Simulation of Plume Rise Model from Multiple Sources," Il Nuovo Cimento, Vol. 5C, No. 4, 1982, pp. 113–130.

[6]Ahmad, N., and Bouhamra, W., "Development of a New Long Term Multiple-Source Plume Model: Applications on Some Industrial and Residential Areas in Kuwait," Environmental Progress, Vol. 12, No. 2, 1993, pp. 123–127.

[7]Meyer, J., Eagles, T., Kohlenstein, L., Kagan, J., and Stanbro, W., "Mechanical-Draft Cooling Tower Visible Plume Behavior: Measurements, Models, Predictions," Cooling Tower Environment—1974, edited by S. Hanna and J. Pell, National Technical Information Service, Springfield, VA, 1975, pp. 307–352.

[8]Davis, L., "Analysis of Multiple Cell Mechanical Draft Cooling Towers," Corvallis Environmental Research Lab., Office of Research and Development, U.S. Environmental Protection Agency, EPA-660/3-75-039, Corvallis, OR, 1975.

[9]Kannberg, L., and Davis, L., "An Experimental/Analytical Investigation of Deep Submerged Multiple Buoyant Jets," U.S. Environmental Protection Agency, EPA 600/3-76-101, Corvallis, OR, Sept. 1976.

[10]Davis, L., and Shirazi, M., "A Review of Thermal Plume Modeling," Corvallis Environmental Research Lab., CERL-048, Office of Research and Development, U.S. Environmental Protection Agency, Corvallis, OR, Sept. 1978.

[11]Macduff, R., and Davis, L., "Multiple Cell Mechanical Draft Cooling Tower Model," Environmental Effects of Atmospheric Heat/Moisture Releases: Cooling Towers, Cooling Ponds, and Area Sources, edited by K. Torrance and R. Watts, American Society of Mechanical Engineers, New York, 1978, pp. 1–8.

[12]Davidson, M., Papps, D., and Wood, I., "The Behaviour of Merging Buoyant Jets," Recent Advances in the Fluid Mechanics of Turbulent Jets and Plumes, edited by P. Davies and M. J. Valente Neves, Kluwer, Dordrecht, The Netherlands, 1994, pp. 465–478.

[13]Wood, I., Bell, R., and Wilkinson, D., "The Behaviour of a Merging Array of Buoyant Jets in a Stationary Uniform Environment," Ocean Disposal of Wastewater, World Scientific, Singapore, 1993, pp. 49–84.

[14]Wood, I., "Asymptotic Solutions and Behavior of Outfall Plumes," Journal of Hydraulic Engineering, Vol. 119, No. 5, 1993, pp. 555–580.

[15]Brog, P., Hofmann, W., Sutter, H., von Euw, H., and Fuchs, H., "Some Developments in Plume and Drift Deposition Modelling Since 1974," Cooling Tower Environment—1978: Proceedings of a Symposium at the Center of Adult Education, University of Maryland, May 2–4, 1978, edited

by R. Nietubicz and R. Green, Water Resources Research Center, Univ. of Maryland, College Park, MD, 1978, pp. III-1–III-23.

[16]Brog, P., "Calculation of Cooling Tower Plumes with KUMULUS," Thermal Effluent from Power Generation, edited by Z. Zaric, Hemisphere, Washington, DC, 1978, pp. 283–293.

[17]Wu, F., and Koh, R., "Mathematical Model for Multiple Cooling Tower Plumes," TR, Corvallis Environmental Research Lab., Office of Research and Development, U.S. Environmental Protection Agency, Corvallis, OR, 1978.

[18]Baum, H., McGrattan, K., and Rehm, R., "Simulation of Smoke Plumes from Large Pool Fires," Proceedings of the 25th International Symposium on Combustion, The Combustion Inst., Pittsburgh, PA, 1994, pp. 1463–1469.

[19]McGrattan, K., Baum, H., and Rehm, R., "Numerical Simulation of Smoke Plumes from Large Oil Fires," Atmospheric Environment, Vol. 30, No. 24, 1996, pp. 4125–4136.

[20]Ghoniem, A., Zhang, X., Knio, O., Baum, H., and Rehm, R., "Dispersion and Deposition of Smoke Plumes Generated from Massive Fires," Journal of Hazardous Materials, Vol. 33, No. 2, 1993, pp. 275–293.

[21]Zhang, X., and Ghoniem, A., "A Computational Model for the Rise and Dispersion of Wind-Blown, Buoyancy Driven Plumes, Part 1. Neutrally Stratified Atmosphere," Atmospheric Environment, Vol. 27, No. 15, 1993, pp. 2295–2311.

[22]Zhang, X., and Ghoniem, A., "A Computational Model for the Rise and Dispersion of Wind-Blown, Buoyancy-Driven Plumes, Part 2. Linearly Stratified Atmosphere," Atmospheric Environment, Vol. 28, No. 18, 1994, pp. 3005–3018.

[23]Zhang, X., and Ghoniem, A., "A Computational Model for the Rise and Dispersion of Wind-Blown, Buoyancy-Driven Plumes, Part 3. Penetration of Atmospheric Inversion," Atmospheric Environment, Vol. 28, No. 18, 1994, pp. 3019–3032.

[24]Rehm, G., and Baum, H., "The Equations of Motion for Thermally Driven, Buoyant Flows," Journal of Research of the National Bureau of Standards, Vol. 83, No. 3, 1978, pp. 297–307.

[25]Pasquill, F., Atmospheric Diffusion, 2nd ed., Halsted, New York, 1974.

[26]Slade, D., "Meteorology and Atomic Energy, 1968," TR, Air Resources Lab., Environmental Science Services Administration, U.S. Dept. of Commerce, Springfield, VA, July 1968.

[27]Panofsky, H., and Dutton, J., Atmospheric Turbulence, Models and Methods for Engineering Applications, Wiley-Interscience, New York, 1984.

[28]Draxler, R., "Determination of Atmospheric Diffusion Parameters," Atmospheric Environment, Vol. 10, No. 2, 1976, pp. 95–105.

[29]Härtel, C., "Turbulent Flows: Direct Numerical Simulation and Large-Eddy Simulation," Handbook of Computational Fluid Mechanics, edited by R. Peyret, Academic Press, London, 1996, Chap. 5, pp. 283–338.

[30]Sweet, R., CRAYFISHPAK User's Guide, Green Mountain Software, Boulder, CO, 1990.